



## Original Article

## Fracture behaviour of fibre-reinforced composite materials subjected to shear loading: An experimental and numerical study

Haibao Liu <sup>a,\*</sup>, Jin Zhou <sup>b</sup>, Xiangshao Kong <sup>c</sup>, Shipeng Li <sup>d</sup><sup>a</sup> Centre for Aeronautics, School of Aerospace, Transport and Manufacturing, Cranfield University, Cranfield MK43 0AL, UK<sup>b</sup> School of Mechanical Engineering, Xi'an Jiaotong University, Xi'an, Shaanxi 710049, China<sup>c</sup> Departments of Naval Architecture, Ocean and Structural Engineering, School of Transportation, Wuhan University of Technology, Wuhan, Hubei 430063, China<sup>d</sup> Key Laboratory of Mechanism Theory and Equipment Design of Ministry of Education, Tianjin University, Tianjin 300350, China

## ARTICLE INFO

## Article history:

Received 24 July 2022

Received in revised form

26 July 2022

Accepted 29 July 2022

Available online 7 August 2022

## Keywords:

Polymer-matrix composites

Shear fracture

Damage mechanisms • finite element analysis

Computational mechanics

## ABSTRACT

Compared to fibre-dominated behaviour, a response dominated by the matrix under shear loading can considerably limit the load-bearing capability and restrict the utilisation of composite materials. It is therefore practically significant to understand the shear response of composite materials. This paper presents a detailed experimental and numerical investigation on the fracture behaviour of composite laminates subjected to shear-dominated loading. Composite specimen with a lay-up of  $[(0/90)_4/0]_S$  are tested using the V-Notched Rail (VRS) shear test method. Subsequently, the Scanning Electron Microscope (SEM) investigation is also conducted on the fracture surfaces of the tested specimens to get insights into the damage mechanisms due to shear loading. In addition, a high-fidelity computational damage model is developed to predict the shear fracture behaviour of fibre-reinforced composites. Simulation results, including loading response, strain distribution and shear fracture, well correlated with experimental results, which demonstrates the predictive capability of the developed elastic-plastic damage model.

© 2022 The Authors. Publishing services by Elsevier B.V. on behalf of KeAi Communications Co. Ltd. This is an open access article under the CC BY-NC-ND license (<http://creativecommons.org/licenses/by-nc-nd/4.0/>).

## 1. Introduction

Composite materials have been increasingly used in the manufacture of a very wide range of structural components, as they can provide excellent mechanical performance [1–3]. Thorough understandings on the failure behaviour of composite materials, subjected to various loading conditions, are required for the design, optimisation and maintenance of composite structures. Among those material properties, in-plane shear modulus and shear strength are of great importance for the design of composite structures [4,5]. Generally, unidirectional (UD) composite laminates present excellent mechanical properties under longitudinal loading, where the response of materials is dominated by carbon-fibres. In contrast, large nonlinear deformation and subsequent matrix cracking, i.e., matrix-dominated failure might be induced under

transverse or shear loading in composite structures. As a key design factor, the shear response and associated fracture behaviours are important design needs to be accurately characterised [6–8].

Many experimental methods are available for evaluating the shear properties of composite materials [9–12]. One of the particular interests is the V-Notched Rail (VRS) test method, that essentially combines the best features of two commonly used methods, the Iosipescu Shear [13,14] (i.e. the generation of a uniform shear stress) and the rail shear test methods.

With the developed testing methods, considerable efforts have been expended in extracting shear properties of composite laminates with different configurations. Almeida Jr. et al. [4] used four testing methods to capture the shear response of glass-fibre reinforced composites. Five composite lay-ups,  $[0]_S$ ,  $[90]_S$ ,  $[0/90/0/90/0]$  and randomly oriented (mat), were employed to investigate the lay-up effects on the in-plane shear response of glass fibre reinforced composites. In these five lay-ups, the randomly oriented lay-up presented higher in-plane shear strength due to its random fibre orientation. The VRS tests described in ASTM Standard D 7078 was adopted by Akats et al. [8] to investigate the influence of ply orientation and notch angle on the in-plane shear properties. Khashaba et al. [15] employed

\* Corresponding author.

E-mail address: [haibao.liu@cranfield.ac.uk](mailto:haibao.liu@cranfield.ac.uk) (H. Liu).

Peer review under responsibility of Editorial Board of International Journal of Lightweight Materials and Manufacture.

composite laminates, which were cut at different off-axis angles, to study the shear behaviour of composite materials. The maximum in-plane shear strength was found for specimens with 45° and 60° off-axis angles, and specimens with 0° and 90° off-axis angles presented the minimum in-plane shear strength in all tested specimens. Based on accurate material characterisation.

The physical testing is essential, but it is also expensive in terms of both time and economy. The demand for a reliable predictive model provides another impetus to investigate the material properties of composite laminates. High-capability numerical tools are able to reduce cost due to physical testing. Furthermore, such tools enable further insight into the complex damage mechanisms. While, comparing to other types of modelling studies like impact or crush modelling, there are limited number of shear modelling studies available. For example, Sun and Rui [16,17] have considered the non-linear stress versus strain curves seen in fibre-reinforced composites as a form of plastic behaviour. They based their non-linear model on an earlier orthotropic elastic-plastic formulation of Kenaga et al. [18] which assumed a yield function that was a quadratic expression with respect to the stresses for a general three-dimensional composite. They also proposed a damage model, based on one-parameter failure criterion, to capture the shear failure behaviour of composites. It was claimed that the matrix-dominant strengths can be accurately predicted by the proposed model. But details like load-displacement trace and damage morphology were not employed to further check the capability of the model in their study, which might be also interesting to investigate.

In this research, we aim to using both the benchmark experimental method and the relatively simple but robust numerical model to investigate the shear fracture behaviour of composite laminates. By doing so, the standard V-notched Rail Shear (VRS) experiments were performed on the fibre-reinforced composite specimens. To get insights into the failure modes of the fractured composite specimens due to shear loading, SEM investigation was also conducted on the fracture surface of the tested specimens. Subsequently, an elastic-plastic damage model, based on the simple flow rule and Northwestern University failure criteria, was employed to simulate the shear experiments. Predicted results, including loading response, strain distribution and shear damage, were compared with the respective experimental results.

## 2. Materials and methods

### 2.1. Specimen preparation

The composite used in this research is manufactured using the unidirectional carbon fibre reinforced epoxy pre-pregs. In detail, 18

layers of pre-pregs were stacked based on a composite lay-up of [(0/90)<sub>4</sub>/0]<sub>S</sub> and then cured in a vacuum environment. The jigs and processing details for the carbon-fibre reinforced epoxy composites are shown in Fig. 1. To ensure the quality of the specimens, all manufactured panels were subsequently inspected using a C-scan device to make sure the pristine specimens were free of any major defects.

The specimen geometry presented in American Society of Testing Materials (ASTM) standard D7078 was adopted in this work. A band saw and a milling cutter were used to machine the profile of the specimen and introduce the V-notch, respectively. The geometry and dimensions of the specimen are shown in Fig. 2 and Table 1, respectively.

### 2.2. Experimental procedure

The shear experiments were performed using an Instron screw-driven testing machine, which has a 150 kN load cell. During the test, displacement control was applied at a crosshead speed of 1 mm/min. To ensure the results consistency, five specimens were tested during the VRS experiments. A Digital Correlation System (DIC) was set up at front of the testing machine to monitor the strain evolution of the VRS specimens. The VRS specimens were speckled using white paints and clamped by a rigid rail-shear fixture during the test. A sub-selection of the tested VRS samples was prepared for the fractographic analysis. Photographs were taken from the fractured VRS specimens first and then the SEM was employed to investigate the fracture surfaces of the tested VRS samples to get insights into the damage mechanisms of composite laminates subjected to shear loading.

## 3. Experimental results

### 3.1. Loading response

Fig. 3 presents the loading response and nominal strengths obtained from the shear experiments performed on the five VRS specimens. Fig. 3a shows the load-displacement curves, where a good consistency was obtained. These load versus displacement curves experienced two main stages: the first stage is the matrix-dominated stage (nonlinear process), and the second is the fibre dominated stage (hardening process). The turning point between two stages is the Initial yielding point. Before reaching the Initial yielding point, tested samples presented nonlinear shear response. By passing the Initial yielding point, the material response reached the hardening process, which is dominated by fibres. The strength

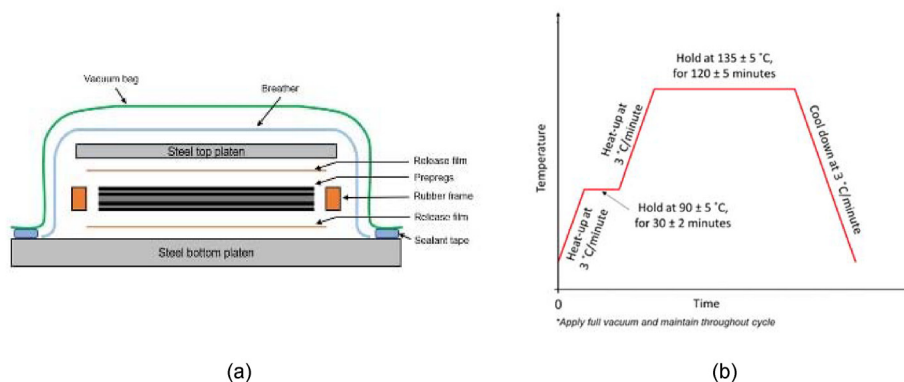


Fig. 1. Diagrams of the consolidation jig and the processing cycle for the carbon fibre/epoxy prepregs: (a) the consolidation jig and (b) the processing cycle.

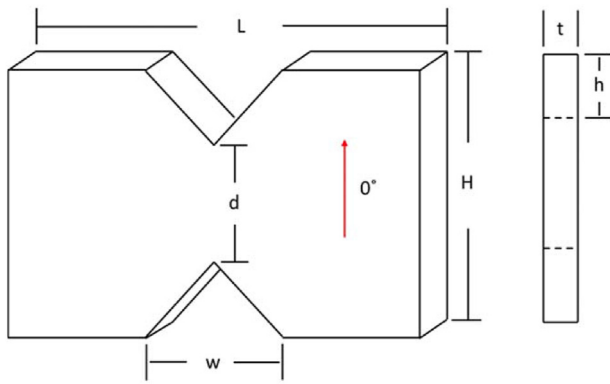


Fig. 2. Dimensions of VRS specimen (all dimensions are in mm).

**Table 1**  
Geometries and lay-ups of VRS specimens (all dimensions are in mm).

Specimen code	Lay-ups	Number of samples	L	H	t	d	w	h
VRS specimens	[(0/90) <sub>4</sub> /0] <sub>s</sub>	5	76	56	2.7	31	25	12.5

corresponding to initial yielding was defined as Initial yielding strength, which is also the maximum load in matrix-dominated stage. The strength corresponding to the maximum load in this fibre-dominated stage was named as hardening strength. Both

initial yielding strength and hardening strength are nominal strength, which can be calculated through:

$$S = \frac{P}{d \times t} \tag{1}$$

where  $S$  is the nominal strength and  $P$  is the load exerted on the shear samples. Terms  $d$  and  $t$  are the distance between two notch tips and the sample thickness, respectively. When  $P$  is equal to the load at initial yielding point, the nominal strength refers to the initial yielding strength. Correspondingly, the hardening strength can be calculated by substituting  $P$  with the maximum load in the hardening procedure. The calculated nominal initial yielding strength and hardening strength are  $150.5 \pm 3\%$  MPa and  $193.5 \pm 5\%$  MPa respectively, shown as Fig. 3b.

### 3.2. Damage morphology

After the shear tests, photographs of fracture surfaces were taken from the tested VRS specimens and shown in Fig. 4. Fibre pull-out, fibre bundle rotation and fibre fracture can be clearly observed from 0° plies which are perpendicular to the loading direction. The 90° plies, which are parallel to the loading direction, presented relatively neat fracture surface due to the nature of matrix fracture. The SEM images obtained from the fracture surface of the VRS specimen is also exhibited in Fig. 4, where failure modes including fibre tensile fracture, fibre pull-out, fibre splitting, fibre debonding and matrix fracture can be observed.

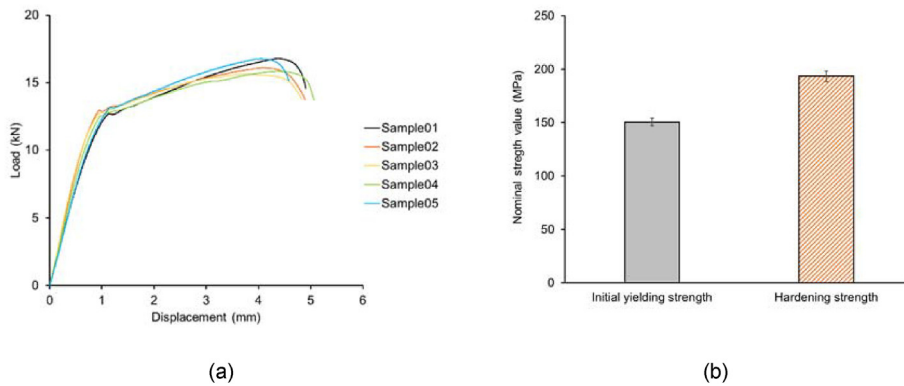


Fig. 3. Loading response and nominal strengths obtained from the shear experiments: (a) the load versus displacement curves and (b) the initial yielding strength and hardening strength.

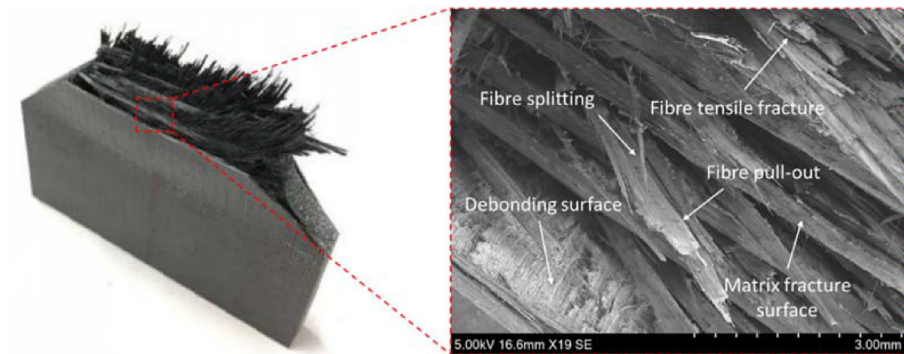


Fig. 4. Photograph and SEM image obtained from the tested VRS specimens: (a) Photograph of the fracture surface and (b) the SEM image showing failure modes due to shear loading.

## 4. Overview of the composite damage model

### 4.1. Introduction

The classical elastic law for the relationships between stress and strain is first considered and then the plastic model based on the quadratic yield criterion is discussed. These two elements are then combined to form the elastic-plastic constitutive relation. A progressive damage model was developed based on the Northwestern University damage criteria and the linear softening law to capture the damage initiation and propagation in the composite laminates. The elastic-plastic constitutive relation and the progressive damage model were then integrated into a Finite Element model to predict the shear-dominated fracture behaviour of fibre-reinforced composite laminates.

### 4.2. The intralaminar damage model

#### 4.2.1. The elastic-plastic constitutive relation

An extended three-dimensional (3-D), elastic-plastic constitutive model [16,17,19–23] has been developed, based on the classic elastic model with the extended plastic model, given by:

$$\begin{pmatrix} d\varepsilon_{11} \\ d\varepsilon_{22} \\ d\varepsilon_{33} \\ d\varepsilon_{12} \\ d\varepsilon_{13} \\ d\varepsilon_{23} \end{pmatrix} = \begin{bmatrix} 1/E_{11} & -\nu_{21}/E_{11} & -\nu_{31}/E_{11} & 0 & 0 & 0 \\ -\nu_{12}/E_{22} & 1/E_{22} & -\nu_{32}/E_{22} & 0 & 0 & 0 \\ -\nu_{13}/E_{33} & -\nu_{23}/E_{33} & 1/E_{33} & 0 & 0 & 0 \\ 0 & 0 & 0 & 1/G_{12} & 0 & 0 \\ 0 & 0 & 0 & 0 & 1/G_{13} & 0 \\ 0 & 0 & 0 & 0 & 0 & 1/G_{23} \end{bmatrix} \begin{pmatrix} d\sigma_{11} \\ d\sigma_{22} \\ d\sigma_{33} \\ d\sigma_{12} \\ d\sigma_{13} \\ d\sigma_{23} \end{pmatrix} + \begin{pmatrix} d\varepsilon_{11}^p \\ d\varepsilon_{22}^p \\ d\varepsilon_{33}^p \\ d\varepsilon_{12}^p \\ d\varepsilon_{13}^p \\ d\varepsilon_{23}^p \end{pmatrix} \quad (2)$$

where  $d\varepsilon_{ij}(i,j = 1, 2, 3)$  and  $d\sigma_{ij}(i,j = 1, 2, 3)$  are the incremental total strain tensors and incremental stress tensors, respectively. The terms  $E_{ij}(i,j = 1, 2, 3)$  and  $G_{ij}(i,j = 1, 2, 3, i \neq j)$  are the Young's moduli shear moduli, respectively. The parameters  $\nu_{ij}(i,j = 1, 2, 3, i \neq j)$  are the Poisson's ratios. The incremental plastic strain tensors,  $d\varepsilon_{ij}^p(i,j = 1, 2, 3)$ , are related to the effective stress,  $\sigma_{eff}$ , and the effective plastic strain,  $\varepsilon_{eff}^p$ . The effective stress,  $\sigma_{eff}$ , is given by:

$$\sigma_{eff} = \sqrt{\frac{3}{2}(\sigma_{22}^2 + \sigma_{33}^2) - 3\sigma_{22}\sigma_{33} + 3a_{44}\sigma_{23}^2 + 3a_{55}\sigma_{13}^2 + 3a_{66}\sigma_{12}^2} \quad (3)$$

where  $a_{44}$ ,  $a_{55}$  and  $a_{66}$  are the anisotropic coefficients. For transversely isotropic elastic solids  $a_{44}$  can be set as two, and  $a_{55}$  equals to  $a_{66}$ , which can be determined from off-axis experiments [16]. A power-law function can be utilised to describe the relation between the effective stress,  $\sigma_{eff}$ , and the effective plastic strain,  $\varepsilon_{eff}^p$ , given by Ref. [16]:

$$\varepsilon_{eff}^p = A\sigma_{eff}^n \quad (4)$$

where  $A$  and  $n$  are the nonlinear coefficients, which can be determined by fitting to the  $\sigma_{eff}$  versus  $\varepsilon_{eff}^p$  data. Thus,  $d\varepsilon_{ij}^p(i,j = 1, 2, 3)$ , can be calculated as:

$$\begin{pmatrix} d\varepsilon_{11}^p \\ d\varepsilon_{22}^p \\ d\varepsilon_{33}^p \\ d\varepsilon_{12}^p \\ d\varepsilon_{13}^p \\ d\varepsilon_{23}^p \end{pmatrix} = \frac{An}{\sigma_{eff}^{1-n}} \begin{pmatrix} 0 \\ 3(\sigma_{22} - \sigma_{33})/2\sigma_{eff} \\ 3(\sigma_{33} - \sigma_{22})/2\sigma_{eff} \\ 3a_{66}\sigma_{12}/2\sigma_{eff} \\ 3a_{66}\sigma_{13}/2\sigma_{eff} \\ 3a_{44}\sigma_{23}/2\sigma_{eff} \end{pmatrix} d\sigma_{eff} \quad (5)$$

#### 4.2.2. Intralaminar damage initiation

In the developed damage model, the three-dimensional (3-D) damage criteria described in Refs. [24–26] are used to predict the onset of the initiation of intralaminar damage, given by:

*Longitudinal failure:*

$$\text{Tension – dominated : } F_{1T} = \left(\frac{\sigma_{11}}{X_T}\right)^2 + \frac{\sigma_{12}^2 + \sigma_{13}^2}{S_{12}^2} \quad (6)$$

$$\text{compression – dominated : } F_{1C} = \left(\frac{\sigma_{11}}{X_C}\right)^2 \quad (7)$$

*Transverse failure ( $|\sigma_{22}| \geq |\sigma_{33}|$ ):*

*Tension – dominated*

$$(|\sigma_{22}| \geq |\tau_{12}(\tau_{23})| \text{ and } \sigma_{22} \geq 0) : F_{2T} = \frac{\sigma_{22}^2}{Y_T} + \left(\frac{E_{22}}{2G_{12}}\right)^2 \left(\frac{\tau_{12}}{Y_T}\right)^2 + \left(\frac{E_{22}}{2G_{23}}\right)^2 \left(\frac{\tau_{23}}{Y_T}\right)^2 \quad (8)$$

*Compression – dominated*

$$(|\sigma_{22}| \geq |\tau_{12}(\tau_{23})| \text{ and } \sigma_{22} \geq 0) : F_{2C} = \left(\frac{\sigma_{22}}{Y_C}\right)^2 + \left(\frac{E_{22}}{G_{12}}\right)^2 \left(\frac{\tau_{12}}{Y_C}\right)^2 + \left(\frac{E_{22}}{G_{23}}\right)^2 \left(\frac{\tau_{23}}{Y_C}\right)^2 \quad (9)$$

*Shear – dominated*

$$(|\sigma_{22}| \leq |\tau_{12}(\tau_{23})|) : F_{2S} = \left(\frac{\tau_{12}}{S_{12}}\right)^2 + \left(\frac{\tau_{23}}{S_{23}}\right)^2 + \frac{2G_{12}\sigma_{22}}{E_{22}Y_C} \leq 1 \quad (10)$$

*Through-thickness failure ( $|\sigma_{33}| \geq |\sigma_{22}|$ ):*

*Tension – dominated*

$$(|\sigma_{33}| \geq |\tau_{13}(\tau_{23})| \text{ and } \sigma_{33} \geq 0) : F_{3T} = \frac{\sigma_{33}^2}{Z_T} + \left(\frac{E_{33}}{2G_{13}}\right)^2 \left(\frac{\tau_{13}}{Z_T}\right)^2 + \left(\frac{E_{33}}{2G_{23}}\right)^2 \left(\frac{\tau_{23}}{Z_T}\right)^2 \quad (11)$$

Compression – dominated

$$(|\sigma_{33}| \geq |\tau_{13}(\tau_{23})| \text{ and } \sigma_{33} \geq 0) : F_{3C} = \left(\frac{\sigma_{33}}{Z_C}\right)^2 + \left(\frac{E_{33}}{G_{13}}\right)^2 \left(\frac{\tau_{13}}{Z_C}\right)^2 + \left(\frac{E_{33}}{G_{23}}\right)^2 \left(\frac{\tau_{23}}{Y_C}\right)^2 \quad (12)$$

Shear – dominated

$$(|\sigma_{33}| \leq |\tau_{13}(\tau_{23})|) : F_{3S} = \left(\frac{\tau_{13}}{S_{13}}\right)^2 + \left(\frac{\tau_{23}}{S_{23}}\right)^2 + \frac{2G_{13}}{E_{33}} \frac{\sigma_{33}}{Z_C} \quad (13)$$

where  $\sigma_{ij}$  is the stress tensor and  $F_{iT}(i = 1, 2, 3)$ ,  $F_{iC}(i = 1, 2, 3)$  and  $F_{iS}(i = 2, 3)$  are the tensile, compressive and shear failure indexes, respectively. The terms  $X_T$ ,  $Y_T$  and  $Z_T$  denote the tensile strengths. Terms  $X_C$ ,  $Y_C$  and  $Z_C$  are the compressive strengths. Finally,  $S_{12}$ ,  $S_{13}$  and  $S_{23}$  refer to the shear strengths.

4.2.3. Intralaminar damage evolution

In the intralaminar damage evolution model, eight damage variables,  $d_{1t}$ ,  $d_{1c}$ ,  $d_{2t}$ ,  $d_{2c}$ ,  $d_{2s}$ ,  $d_{3t}$ ,  $d_{3c}$  and  $d_{3s}$ , were defined, to indicate the damage evolution, noting that  $\gamma_{ij} = 2\epsilon_{ij}$ . A general form of the damage variables is given by Ref. [27]:

$$d = \frac{\epsilon^f (\epsilon - \epsilon^0)}{\epsilon (\epsilon^f - \epsilon^0)} \quad (14)$$

The strain,  $\epsilon$ , is the equivalent strain in the composite ply. The strain values,  $\epsilon^0$  and  $\epsilon^f$ , are the equivalent strains corresponding to the initiation of damage and final failure, respectively. The tensors,  $\epsilon_{ij}^f (i, j = 1, 2, 3)$ , refer to the final failure strains. To degrade the elasticity matrix and the resulting stresses, damage parameters,  $d_1$ ,  $d_2$ ,  $d_3$  and  $d_s$ , are defined to reflect the evolution of the longitudinal, transverse, through-thickness and shear damage, respectively, which can be derived as follows [27]:

$$\text{Longitudinal damage} : d_1 = \begin{cases} d_{1t}, & \text{and } \sigma_{11} \geq 0 \\ d_{1c}, & \text{and } \sigma_{11} \leq 0 \end{cases} \quad (15)$$

$$\text{Transverse damage} : d_2 = \begin{cases} d_{2t}, & |\sigma_{22}| \geq |\sigma_{12}(\sigma_{23})| \text{ and } \sigma_{22} \geq 0 \\ d_{2c}, & |\sigma_{22}| \geq |\sigma_{12}(\sigma_{23})| \text{ and } \sigma_{22} \leq 0 \\ d_{2s}, & |\sigma_{22}| \leq |\sigma_{12}(\sigma_{23})| \end{cases} \quad (16)$$

Through – thickness damage :

$$d_3 = \begin{cases} d_{3t}, & |\sigma_{33}| \geq |\sigma_{13}(\sigma_{23})| \text{ and } \sigma_{33} \geq 0 \\ d_{3c}, & |\sigma_{33}| \geq |\sigma_{13}(\sigma_{23})| \text{ and } \sigma_{33} \leq 0 \\ d_{3s}, & |\sigma_{33}| \leq |\sigma_{13}(\sigma_{23})| \end{cases} \quad (17)$$

$$\text{Shear damage} : d_s = 1 - (1 - d_1)(1 - d_2)(1 - d_3) \quad (18)$$

The damage parameters,  $d_1$ ,  $d_2$ ,  $d_3$  and  $d_s$ , were then used to update the elasticity matrix and also determine the resulting stress during the simulation. For more details of this composite model, please refer to Ref. [28].

4.3. The interlaminar damage model

An elastic constitutive relation was employed to capture the response prior to delamination and a quadratic-stress criterion was used to govern the initiation of delamination [27,29–31]. This criterion states that initiation of delamination damage occurs when:

$$\left(\frac{t_{33}}{t_{33}^0}\right)^2 + \left(\frac{t_{31}}{t_{31}^0}\right)^2 + \left(\frac{t_{32}}{t_{32}^0}\right)^2 = 1 \quad (19)$$

where the term  $t_i (i = 33, 31, 32)$  represents the current normal or shear stresses and  $t_i^0 (i = 33, 31, 32)$  represents the normal and shear cohesive strengths. The corresponding displacements are denoted by  $\delta_{33}$ ,  $\delta_{31}$  and  $\delta_{32}$ , and by  $\delta_{33}^0$ ,  $\delta_{31}^0$  and  $\delta_{32}^0$ , respectively.

The energy-based Benzeggagh-Kenane (B–K) [32,33] criterion for propagation of the mixed-mode delamination was used to derive a total value  $G_c$  for the growth of the delamination between the composite plies and is given by:

$$G_c = G_{Ic} + (G_{IIc} - G_{Ic}) \left(\frac{G_{II} + G_{III}}{G_I + G_{II} + G_{III}}\right)^\eta \quad (20)$$

where  $G_{Ic}$  is the Mode I (opening tensile),  $G_{IIc}$  is the Mode II (in-plane shear) interlaminar fracture energy, and  $\eta$  is the B–K Mixed-mode interaction exponent. The values of  $G_{Ic}$ ,  $G_{IIc}$  and  $\eta$  can be experimentally measured [32–35]. The parameters  $G_I$ ,  $G_{II}$  and  $G_{III}$  are the current Mode I, Mode II and Mode III (anti-plane shear) energy-release rates, respectively.

5. Finite element model

5.1. Model definition

The finite element (FE) model was created in Abaqus 2018, in which 1 mm × 1 mm C3D8R elements were employed in the

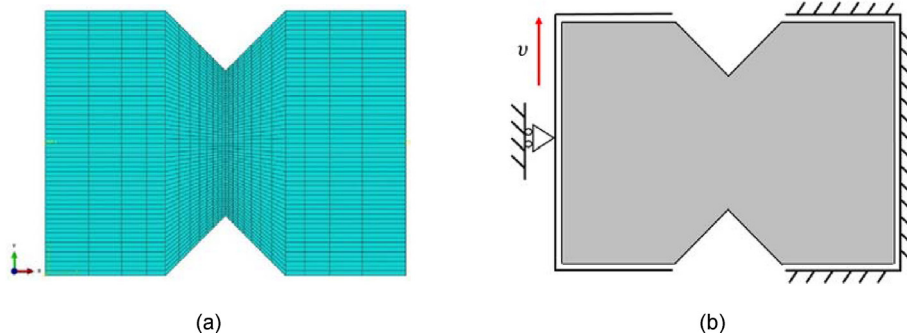
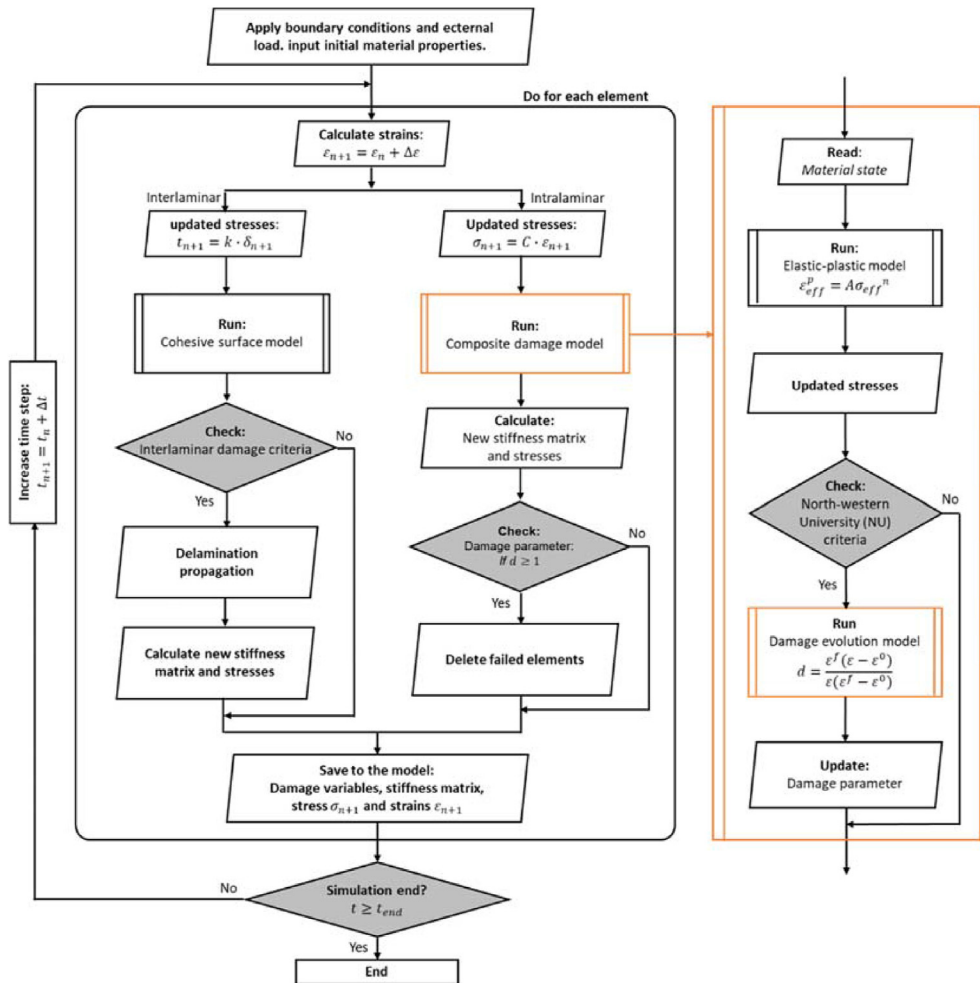


Fig. 5. The virtual specimen and boundary condition defined in the shear simulation: (a) the virtual shear specimen and (b) the boundary condition employed in the simulation.



**Table 2**  
Properties of composite materials used for model validation [19,36].

Property	CF/Epoxy curved panel
Moduli (GPa)	$E_{11} = 127; E_{22} = E_{33} = 8.4; G_{23} = 4.2; G_{12} = G_{13} = 4.2$
Poisson's ratio	$\nu_{23} = 0.31; \nu_{12} = \nu_{13} = 0.31$
Strength values (MPa)	$X^T = 2200; Y^T = Z^T = 49;$ $X^C = 1470; Y^C = Z^C = 199; S^L = 154$
Ply fracture energies (kJ/m <sup>2</sup> )	$G_{Ic _{fc}} = 108; G_{Ic _{fc}} = 58; G_{Ic _{mc}} = 0.5; G_{Ic _{mc}} = 1.6$
Interlaminar fracture energies+(kJ/m <sup>2</sup> )	$G_{Ic} = 0.5; G_{IIc} = 1.6$
Benzeggagh–Kenane exponent	$\eta_{BK} = 1.21$
Cohesive strengths (MPa)	$\sigma_n^0 = 54.0; \tau_s^0 = \tau_t^0 = 70$
Cohesive law stiffness (MPa/mm)	$k = 1.4 \times 10^6$
Nonlinear coefficients	$a_{66} = 2.7; A = 3.14 \times 10^{-13} \text{ MPa}^{-n}; n = 4.19$



**Fig. 6.** The implementation of the FE numerical model showing schematically the flow charts, for one computational time-step and for a single element. With both the flowchart for the main model and the flow-chart for the elastic-plastic damage model shown.

central area as shown in Fig. 5a, to deliver results with good accuracy whilst ensure the computation efficiency. The finite element model, created for shear simulation, has 26,312 elements. The boundary condition was defined according to the set-up in the shear experiments and shown in Fig. 5b. In the simulation, the general contact algorithm is used to govern the global contact. Friction coefficient of 0.25 is defined for the composite/composite contact, respectively. Computations were completed using 16 CPUs on a Linux Cluster with a run time of 12–15 h.

5.2. Input parameters

In this research, the unidirectional carbon fibre reinforced epoxy composite specimens were tested to investigate the shear failure behaviour of composite laminates. The basic mechanical properties of the unidirectional composite ply, including strengths, moduli and fracture toughness etc., were obtained from in-house characterisations and literatures [36]. The nonlinear parameters reported in Ref. [19] were taken for this carbon fibre epoxy composites here.

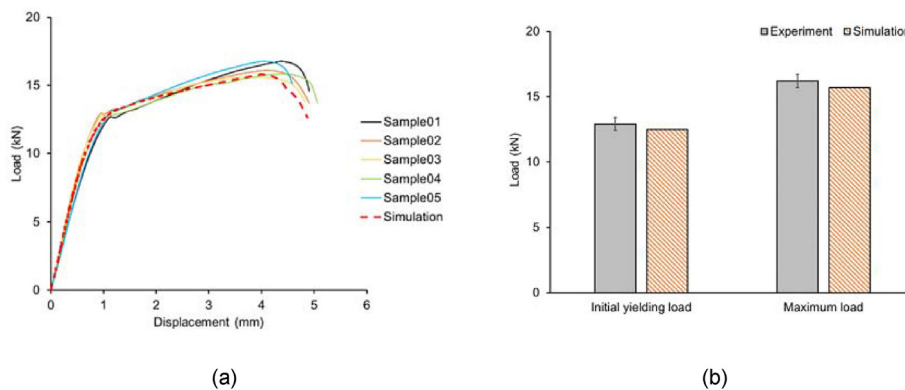


Fig. 7. Comparison of experimental and numerical load versus displacement curves obtained from (a) standard (b) single-blocked and (c) double-blocked shear samples.

The input parameters required for the developed finite element model are presented in Table 2.

### 5.3. Model implementation

The flow-chart of the finite element model is schematically shown in Fig. 6, giving a typical computation step for a single element. The computation process was performed for every appropriate single element in the finite element model for elastic-plastic behaviour of composite laminates.

## 6. Comparison between experimental and numerical results

### 6.1. Loading response

The load versus displacement curves and the initial yielding load as well as the maximum load obtained from experiment and simulation are compared in Fig. 7. Computational load versus displacement trace was extracted from the simulation results and compared those load versus displacement curves obtained from VRS specimens in Fig. 7a, where both the computational and experimental curves firstly increased following a larger gradient prior to the initial yielding point, after which a hardening procedure with a lower gradient was presented. It can be found the developed computational model is able to reasonably capture the loading response of the composite specimens under shear-dominated loading. To further check the predictive capability of

the model, the initial yielding load and the maximum load were also extracted from the simulation results and compared with the experimental ones, Fig. 7b. Compared to experimental initial yielding load and the maximum load (12.9 kN and 16.2 kN respectively), even though the simulation results showed a relatively lower values for these two measurements (12.5 kN and 15.7 kN respectively), the differences between the experimental and numerical values are smaller than 6% for both the initial yielding load and the maximum load, which demonstrates a good agreement between the experimental measurements and numerical predictions.

### 6.2. Strain distribution

Fig. 8 presents the strain distribution maps extracted from the shear experiments and simulation performed on the VRS specimens. For comparison, the initial strain rates of these specimens were also attached with the strain distribution obtained at  $d = 1$  mm during the shear testing. Fig. 8a shows the strain maps measured using the DIC system when  $d = 0$  mm and  $d = 1$  mm during the shear experiments. It can be seen that, when  $d = 1$  mm, strain concentration appeared along the ligament of the shear specimen due to the shear loading. Similarly, a clear strain concentration zone was also observed from the simulation results presented in Fig. 8b. Good correlation was achieved between the experimental and numerical results.

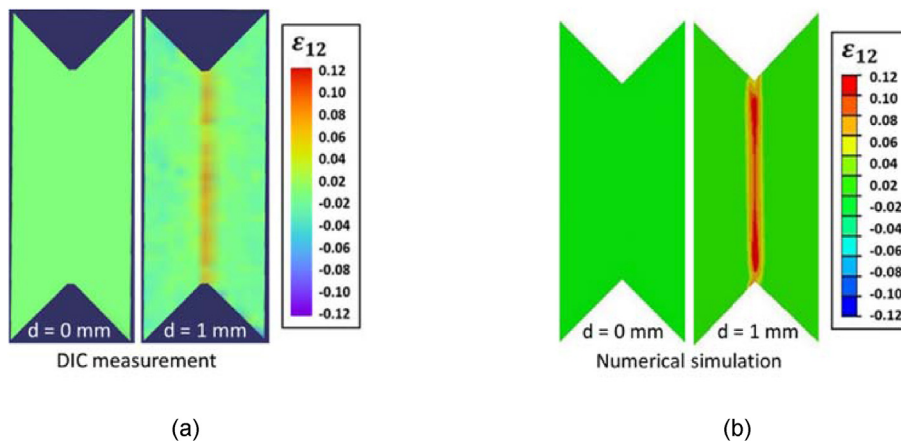


Fig. 8. Comparison of strain distribution obtained from experiment and simulation at  $t = 0$  s and  $t = 30$  s: (a) the DIC measurement and (b) the numerical simulation results.

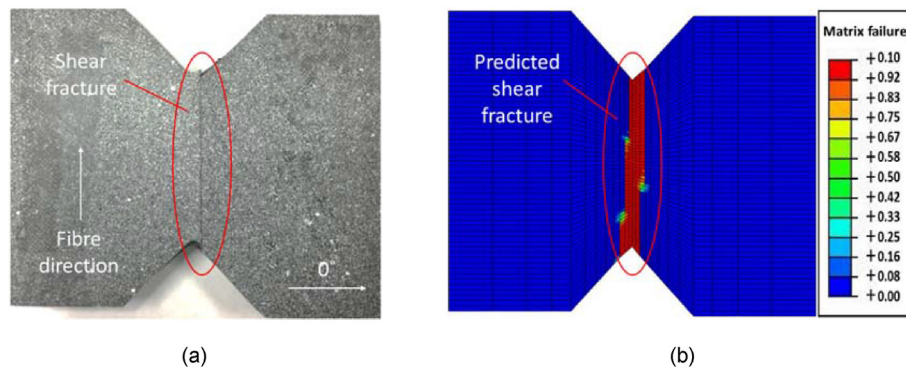


Fig. 9. Photograph of shear fracture failure obtained from the experimental and computational results: (a) physically tested specimen and (b) virtually tested specimen.

### 6.3. Shear fracture

Fig. 9 shows the shear fracture failure obtained VRS experiment and simulation. Fig. 9a shows a photograph taken from the fractured VRS specimen. The outer ply of specimen is in  $90^\circ$  direction. As shown in the figure, a through crack formed along the ligament of the VRS specimen due to the shear loading. Correspondingly, a fracture band was observed from the virtual VRS specimen and shown in Fig. 9b. This accordance between the experimental and numerical results demonstrates that the developed damage model can accurately predict the stress concentration and the subsequent fracture due to the shear loading.

### 7. Conclusions

The shear response of composite laminates plays an important role in the design of composite structures. This research presents a detailed experimental and numerical investigation on the shear failure behaviour of composite materials. For the experimental investigation, composite specimens with a lay-up of  $[(0/90)_4/0]_s$  were manufactured and tested based on the ASTM D7078/D7078M – 05 standard. Experimental results, including loading response and damage morphology, were obtained and analysed to understand the damage mechanisms of the composite laminates subjected to the shear-dominated loading. The loading versus displacement traces showed that composite specimens experienced obvious nonlinear process when subjected shear-dominated loading. The Scanning Electron Microscope (SEM) images showed that a series of failure modes such as fibre pull-out/breakage, matrix cracking and delamination et al. were presented by the fractured shear specimens. In the numerical investigation, an elastic-plastic damage model was employed to simulate the V-notched Rail Shear (VRS) experiments performed on the composite laminates. The simulation results, including loading response, strain distribution and shear-induced damage, yielded good agreement to the experimental results.

### Conflicts of interest

The authors declare that they have no known competing financial interests or personal relationships that could have appeared to influence the work reported in this paper.

### Acknowledgements

Supports from the Research Computing Team at Cranfield University in accessing the high-performance computing facilities are gratefully acknowledged.

### References

- [1] D. Hull, T.W. Clyne, *An Introduction to Composite Materials*, Cambridge University Press, 1996.
- [2] H. Liu, J. Liu, C. Kaboglu, H. Chai, X. Kong, B.R.K. Blackman, A.J. Kinloch, J.P. Dear, Experimental investigations on the effects of projectile hardness on the impact response of fibre reinforced composite laminates, *Int. J. Light. Mater. Manuf.* 3 (2019) 77–87.
- [3] A.B. de Moraes, Open-hole tensile strength of quasi-isotropic laminates, *Compos. Sci. Technol.* 60 (2000) 1997–2004.
- [4] JHSA, C.C. Angrizani, E.C. Botelho, S.C. Amico, Effect of fiber orientation on the shear behavior of glass fiber/epoxy composites, *Mater. Des.* 65 (2015) 789–795.
- [5] H. Liu, J. Liu, C. Kaboglu, J. Zhou, X. Kong, B.R.K. Blackman, A.J. Kinloch, J.P. Dear, The behaviour of fibre-reinforced composites subjected to a soft impact-loading: An experimental and numerical study, *Eng. Fail. Anal.* 111 (2020), 104448.
- [6] R.K. Joki, A.F. Grytten, B. Hayman, Nonlinear response in glass fibre non-crimp fabric reinforced vinylester composites, *Compos. B Eng.* 77 (2015) 105–111.
- [7] R.B. Williams, *Nonlinear Mechanical and Actuation Characterization of Piezoceramic Fiber Composites*, 2004.
- [8] M. Aktas, M.E. Deniz, Determination of in-plane shear properties of composite laminates, *Electron. J. Mach. Technol.* 7 (2010) 13–23.
- [9] ASTM, *Standard Test Method for In-Plane Shear Properties of Polymer Matrix Composite Materials by the Rail Shear Method*, 2014. D4255/D4255M-14, West Conshohocken, PA.
- [10] ASTM, *Standard Test Method for Short-Beam Strength of Polymer Matrix Composite Materials and Their Laminates*, 2016. D2344/D2344M-16, West Conshohocken, PA.
- [11] ASTM, *Standard Test Method for In-Plane Shear Response of Polymer Matrix Composite Materials by Tensile Test of a  $\pm 45^\circ$  Laminate*, 2014. D3518/D3518M-14, West Conshohocken, PA.
- [12] ASTM, *Standard Test Method for Shear Properties of Composite Materials by V-Notched Rail Shear Method*, 2014. D7078/D7078M-14, West Conshohocken, PA.
- [13] ASTM, *Standard Test Method for Shear Properties of Composite Materials by the V-Notched Beam Method*, 2012. D5379/D5379M-12, West Conshohocken, PA.
- [14] G. Catalanotti, J. Xavier, Measurement of the mode II intralaminar fracture toughness and R-curve of polymer composites using a modified Iosipescu specimen and the size effect law, *Eng. Fract. Mech.* 138 (2015) 202–214.
- [15] U.A. Khashaba, In-plane shear properties of cross-ply composite laminates with different off-axis angles, *Compos. Struct.* 65 (2004) 167–177.
- [16] C.T. Sun, J.L. Chen, A simple flow rule for characterizing nonlinear behavior of fiber composites, *J. Compos. Mater.* 23 (1989) 1009–1020.
- [17] C.T. Sun, Y. Rui, Orthotropic elasto-plastic behavior of AS4/PEEK thermoplastic composite in compression, *Mech. Mater.* 10 (1990) 117–125.
- [18] D. Kenaga, J.F. Doyle, C.T. Sun, The characterization of boron/aluminum composite in the nonlinear range as an orthotropic elastic-plastic, *Material. J. Compos. Mater.* 21 (1987) 516–531.
- [19] T. Yokozeki, S. Ogihara, S. Yoshida, T. Ogasawara, Simple constitutive model for nonlinear response of fiber-reinforced composites with loading-directional dependence, *Compos. Sci. Technol.* 67 (2007) 111–118.
- [20] T.S. Gates, C.T. Sun, Elastic/viscoplastic constitutive model for fiber reinforced thermoplastic composites, *AIAA J.* 29 (1991) 457–463.
- [21] J.K. Chen, F.A. Allahdadi, C.T. Sun, A quadratic yield function for fiber-reinforced composites, *J. Compos. Mater.* 31 (1997) 788–811.
- [22] C.A. Weeks, C.T. Sun, Modeling non-linear rate-dependent behavior in fiber-reinforced composites, *Compos. Sci. Technol.* 58 (1998) 603–611.
- [23] K.J. Yoon, C.T. Sun, Characterization of elastic-viscoplastic properties of an AS4/PEEK thermoplastic composite, *J. Compos. Mater.* 25 (1991) 1277–1296.



- [24] I.M. Daniel, J. Luo, P.M. Schubel, Three-dimensional characterization of textile composites 39, 2008, pp. 13–19.
- [25] I.M. Daniel, J. Luo, P.M. Schubel, B.T. Werner, Interfiber/interlaminar failure of composites under multi-axial states of stress, *Compos. Sci. Technol.* 69 (2009) 764–771.
- [26] I.M. Daniel, Failure of composite materials, *Strain* 43 (2007) 4–12.
- [27] D. Systèmes, Abaqus 2018 Documentation, English Version, 2018.
- [28] H. Liu, J. Liu, Y. Ding, Z.E. Hall, X. Kong, J. Zhou, B.R.K. Blackman, A.J. Kinloch, J.P. Dear, A three-dimensional elastic-plastic damage model for predicting the impact behaviour of fibre-reinforced polymer-matrix composites, *Compos. B Eng.* 201 (2020), 108389.
- [29] J. Brewer, P. Lagace, Quadratic stress criterion for initiation of delamination, *J. Compos. Mater.* 22 (1988) 1141–1155.
- [30] A. Turon, C. Davila, P. Camanho, J. Costa, An engineering solution for mesh size effects in the simulation of delamination using cohesive zone models, *Eng. Fract. Mech.* 74 (2007) 1665–1682.
- [31] A. Turon, P. Camanho, J. Costa, J. Renart, Accurate simulation of delamination growth under mixed-mode loading using cohesive elements: definition of interlaminar strengths and elastic stiffness, *Compos. Struct.* 92 (2010) 1857–1864.
- [32] P. Camanho, C. Davila, M. De Moura, Numerical simulation of mixed-mode progressive delamination in composite materials, *J. Compos. Mater.* 37 (2003) 1415–1438.
- [33] M. Benzeggagh, M. Kenane, Measurement of mixed-mode delamination fracture toughness of unidirectional glass/epoxy composites with mixed-mode bending apparatus, *Compos. Sci. Technol.* 56 (1996) 439–449.
- [34] C. Sarrado, A. Turon, J. Renart, I. Urresti, Assessment of energy dissipation during mixed-mode delamination growth using cohesive zone models, *Compos. Part A Appl. Sci. Manuf.* 43 (2012) 2128–2136.
- [35] S. Hashemi, A. Kinloch, J. Williams, The analysis of interlaminar fracture in uniaxial fibre-polymer composites, *Proc. R. Soc. London. A. Math. Phys. Sci.* 427 (1990) 173–199.
- [36] P. Feraboli, B. Wade, F. Deleo, M. Rassaian, M. Higgins, A. Byar, LS-DYNA MAT54 modeling of the axial crushing of a composite tape sinusoidal specimen, *Compos. Part A Appl. Sci. Manuf.* 42 (2011) 1809–1825.